

1     **Insights into the significant increase of ozone during COVID-**  
2                   **19 in a typical urban city of China**

3  
4     **Kun Zhang**<sup>a, b#</sup>, **Zhiqiang Liu**<sup>a, c#</sup>, **Xiaojuan Zhang**<sup>a, c</sup>, **Qing Li**<sup>a, b</sup>, **Andrew Jensen**<sup>d, e</sup>, **Wen Tan**<sup>f</sup>,  
5                   **Ling Huang**<sup>a, b</sup>, **Yangjun Wang**<sup>a, b</sup>, **Joost de Gouw**<sup>d, e</sup>, **Li Li**<sup>a, b\*</sup>

6     <sup>a</sup> School of Environmental and Chemical Engineering, Shanghai University, Shanghai, 200444, China

7     <sup>b</sup> Key Laboratory of Organic Compound Pollution Control Engineering, Shanghai University,  
8     Shanghai, 200444, China

9     <sup>c</sup> Changzhou Institute of Environmental Science, Changzhou, Jiangsu, 213022, China

10    <sup>d</sup> Cooperative Institute for Research in Environmental Sciences, University of Colorado, Boulder,  
11    Colorado, 80309, USA

12    <sup>e</sup> Department of Chemistry, University of Colorado, Boulder, Colorado, 80309, USA

13    <sup>f</sup> Tofwerk AG, Thun, Switzerland

14    # These authors contribute equally to this work.

15

16    *Correspondence:* Li Li (lily@shu.edu.cn)

17

18    **Abstract**

19        The outbreak of COVID-19 promoted strict restrictions to human activities in China, which led to  
20    dramatic decrease in most air pollutant concentrations (e.g., PM<sub>2.5</sub>, PM<sub>10</sub>, NO<sub>x</sub>, SO<sub>2</sub>, and CO).  
21    However, obvious increase of ozone (O<sub>3</sub>) concentrations was found during the lockdown period in  
22    most urban areas of China. In this study, we conducted a field measurement targeting ozone and its  
23    key precursors by utilizing a novel proton transfer reaction time-of-flight mass spectrometer (PTR-  
24    TOF-MS) in Changzhou, which is representative for the Yangtze River Delta (YRD) city cluster of  
25    China. We further applied the integrated methodology including machine learning, observation-based  
26    model (OBM), and sensitivity analysis to get insights into the reasons causing the obvious increase of

27 ozone. Major findings include: (1) By deweathered calculation, we found changes in precursor  
28 emissions contributed 1.46 ppbv to the increase in the observed O<sub>3</sub> during the Full-lockdown period in  
29 2020, while meteorology constrained 3.0 ppbv of O<sub>3</sub> in the Full-lockdown period of 2019. (2) By  
30 using an OBM model, we found that although significant reduction of O<sub>3</sub> precursors was observed  
31 during Full-lockdown period, the photochemical formation of O<sub>3</sub> was stronger than that during the  
32 Pre-lockdown period. (3) The NO<sub>x</sub>/VOCs ratio dropped dramatically from 1.84 during Pre-lockdown  
33 to 0.79 in Full-lockdown period, which switched O<sub>3</sub> formation from VOCs-limited regime to the  
34 boundary of NO<sub>x</sub>- and VOC-limited regime. Additionally, box model results suggested that the  
35 decrease in NO<sub>x</sub>/VOCs ratio during Full-lockdown period could increase the MeanO<sub>3</sub> by 2.4 ppbv.  
36 Results of this study give insights into the relationship between O<sub>3</sub> and its precursors in urban area,  
37 and demonstrate reasons causing the obvious increase of O<sub>3</sub> in most urban areas of China during the  
38 COVID-19 lock-down period. This study also underlines the necessity of controlling anthropogenic  
39 OVOCs, alkenes, and aromatics in the sustained campaign of reducing O<sub>3</sub> pollution in China.

40 **Keywords:** Ozone; VOCs; PTR-TOF-MS; COVID-19

## 41 **1. Introduction**

42 At the end of 2019, a tragic coronavirus (COVID-19) occurred, which has caused over 271  
43 million global infection and over 4.51 million deaths as of this writing (12<sup>th</sup> Feb 2022). To protect  
44 people's health, China adopted strict measures to control the spread of this pandemic. Thirty provinces,  
45 autonomous regions and municipalities have launched Full-lockdown response (also known as Level I  
46 response, roughly from 24<sup>th</sup> Jan to 25<sup>th</sup> Feb 2020) as early as 24<sup>th</sup> Jan 2020 (Shen et al., 2021; Li et al.,  
47 2020; Huang et al., 2020). With the effective control of COVID-19 in China, the emergency response  
48 level in most provinces (except Hubei province, the hardest-hit region) gradually downgraded to  
49 Partial-lockdown (Level II and Level III response, roughly after 25<sup>th</sup> Feb 2020) (Li et al., 2020), and  
50 work resumption started. During Full-lockdown period, all the social events that may cause crowds  
51 (excluding transportation and industries that maintained the basic operation of society) were severely  
52 restricted. Affected by the pandemic, many factories were shut down, and the on-road traffic volume

53 and construction activities have been reduced significantly (Zheng et al., 2020). During Full-lockdown  
54 period, dramatic decrease of air pollutants (e.g., PM<sub>2.5</sub>, NO<sub>2</sub>, BC) were found in China, especially in  
55 urban areas (Fan et al., 2021; Gao et al., 2021; Li et al., 2020; Xu et al., 2020). Surprisingly, marginal  
56 increases of O<sub>3</sub> were observed during the lockdown period in YRD region, and this seems to be  
57 contradictory to the decrease of most air pollutants (Li et al., 2020). However, as suggested by  
58 previous studies, the formation of O<sub>3</sub> is significantly influenced by NO<sub>x</sub>/VOCs ratio and  
59 meteorological conditions (temperature, relative humidity and actinic flux) (Zhang et al., 2020a;  
60 Zhang et al., 2020b). Therefore, it is essential to investigate the changes of meteorological and  
61 emissions conditions to figure out reasons causing the increase of O<sub>3</sub> during this pandemic.

62 Previous studies on the O<sub>3</sub> pollution in the YRD region have often focused on the more populated  
63 metropolitan areas, such as Shanghai and Nanjing, which are considerably far away from the  
64 industrial zones that are essentially responsible for the sources of O<sub>3</sub> precursors (Li et al., 2019; Zhang  
65 et al., 2020b). Changzhou, located in the center of the Yangtze River Delta (YRD) region, is a typical  
66 city with fast urbanization, heavy industrial structure, huge energy consumption, increasing vehicle  
67 stocks and frequent air pollution. Therefore, it provides a more representative environment to fully  
68 elucidate the mechanism underlying the O<sub>3</sub> pollution in the YRD region (Shi et al., 2020). In a  
69 companion paper (Jensen et al., 2021), we also demonstrated that Changzhou is representative for the  
70 region by analyzing both surface observations and satellite data. According to previous studies, the  
71 anthropogenic VOCs emission in Changzhou was around 9~12.6×10<sup>4</sup> tons/year, among which  
72 industries was the dominant source, accounting for 27~47% of the total VOC emissions (Cheng et al.,  
73 2016; Fu et al., 2013). It is notable that industrial sources together contributed over 80% of  
74 anthropogenic VOC emissions (Sun et al., 2019). Apart from industrial sources, vehicle exhaust  
75 accounted for 9%~14% of total VOC emissions (Sun et al., 2019). However, rare observation  
76 regarding VOCs characteristics during COVID-19 in Changzhou has been conducted.

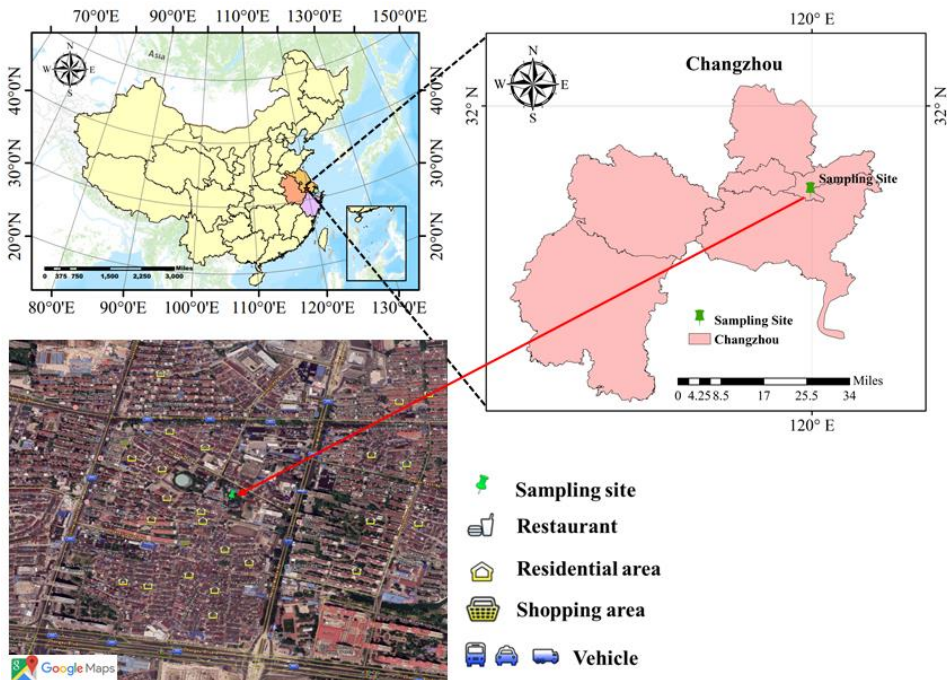
77 Highly time-resolved measurements of VOCs are generally much sparse and could not be easily  
78 expanded during the lockdowns. This limits our understanding of how VOCs changed and how the  
79 formation of ozone was affected. Here, we used a novel proton transfer reaction time-of-flight mass

80 spectrometer (PTR-TOF-MS, ToFwerk, Model Vocus Elf, CHE) to conduct online observation of  
81 VOCs in Changzhou. The characteristics of VOCs and the variations of general air pollutants in each  
82 emergency response period were analyzed. Additionally, ozone formation during each period was  
83 investigated by an OBM model. Although terrifying impact has been caused by the COVID-19, it  
84 provided a rare experiment to analyze the variations of VOCs and NO<sub>x</sub> due to changes of  
85 anthropogenic activities in a typical city of China. Furthermore, results of this study offer theoretical  
86 support for formulating refined ozone management policy in China.

## 87 **2. Methodology**

### 88 **2.1 Field measurement**

89 The field campaign was conducted from 8<sup>th</sup> Jan to 31<sup>st</sup> Mar 2020 at a sampling site located on the  
90 rooftop of a building at Changzhou Environmental Monitoring Center (CEMC, 31.76° N, 119.96° E),  
91 which was approximately 15 m above ground level. As a typical urban monitoring station, this site is  
92 in the center of Changzhou city, surrounded by residential and commercial area, which is also adjacent  
93 to the main transportation junction in Changzhou (Figure 1). According to local epidemic prevention  
94 policies, we roughly classified the measurement periods into three stages: Pre-lockdown (8<sup>th</sup> January  
95 to 23<sup>rd</sup> January 2020), Full-lockdown (25<sup>th</sup> January to 24<sup>th</sup> February 2020), Partial-lockdown (25<sup>th</sup>  
96 February to 28<sup>th</sup> March 2020) as defined in a study of the Yangtze River Delta (Li Li et al., 2020).



97  
98 **Figure 1. Location of the sampling site in Changzhou.**

99 From Jan 8<sup>th</sup> to Mar 27<sup>th</sup>, 2020, the concentrations of traditional air pollutants (PM<sub>2.5</sub>, PM<sub>10</sub>, NO<sub>x</sub>,  
100 SO<sub>2</sub>, CO, O<sub>3</sub>) as well as meteorological parameters were monitored by a series of analyzers (Table  
101 **1Error! Reference source not found.**). In particular, 87 VOCs species were quantified, 59 of which  
102 were identified, by a PTR-TOF-MS with time resolution of 1 min. Detailed measurement techniques  
103 and quality assurance and control has been documented in detail in our companion paper (Jensen et al.,  
104 2021). Here, we just briefly introduce the measurement. The air samples were directly drawn into a 3  
105 m-long tube connected to the instrument. A priming pump, with flow rate of 4 L/min, was used to  
106 reduce the retention time of the gas sample in the tube. To avoid blocking of inlet tube caused by  
107 particles, a particulate filter was assembled at the front of the inlet tube. The pressure of the ion source  
108 was set as 2 mbar and the temperature of the reaction chamber was set to 90 °C during the observation.  
109 VOCs are ionized by reactions with H<sub>3</sub>O<sup>+</sup> ions from a discharge, and the product ions are detected by  
110 a time-of-light mass analyzer (m/Δm FMHW of 950 at m/Q 107). The PTR-TOF-MS can detect most  
111 unsaturated hydrocarbons and VOCs with functional groups but cannot detect species with proton  
112 affinities lower than that of water, namely alkanes and small alkenes. Eighteen standard gases  
113 (including acetonitrile, acetaldehyde, acrolein, acetone, isoprene, butanone, 2-butanone, benzene, 2-

114 pentanone, ethyl acetate, toluene, methyl isobutyl ketone, styrene, xylene, trimethylbenzene,  
115 naphthalene,  $\alpha$ -pinene, and 1,3-dichlorobenzene) with concentrations of 1 ppmv were used for the  
116 calibration of the PTR-TOF-MS. In addition, a built-in calibration system was used to control the zero  
117 and standard gases.

118

**Table 1 Measurements performed during the field campaign.**

Species/Parameter	Experimental Technique
T, RH, WS, WD and P	2000WX, Airmax, USA
O <sub>3</sub>	400E, API, USA
NO <sub>x</sub> (NO and NO <sub>2</sub> )	T200, API, USA
SO <sub>2</sub>	T100, API, USA
CO	T300, API, USA
PM <sub>2.5</sub>	5030, Thermo Fisher, USA
PM <sub>10</sub>	5030, Thermo Fisher, USA
VOCs	Vocus Elf, Tofwerk, CHE

119

## 120 2.2 Observation-based model

121 An OBM model coupled with MCM v3.3.1 was utilized to investigate the atmospheric oxidation  
122 capability and the radical chemistry. Detailed information about the chemistry mechanism is available  
123 on MCM website (<http://mcm.leeds.ac.uk/MCM/>, last access 8 Jul 2021). More than 5800 chemical  
124 species and 17000 reactions are included in this mechanism. The photolysis frequencies (J values)  
125 were calculated as a function of solar zenith angle, altitude using lookup tables, calculated using the  
126 Tropospheric Ultraviolet and Visible (TUV) model (Wolfe et al., 2016). Dilution mixing within the  
127 boundary layer is considered. However, as a 0-D model, vertical or horizontal transport of airmasses  
128 are not involved. The observed meteorological parameters (T, RH, P), trace gases (NO, NO<sub>2</sub>, CO, SO<sub>2</sub>,  
129 and VOCs) were used to constrain the model. Before each simulation, the model was run 3 days as  
130 spin-up to reach a stable state. According to the definition of atmospheric oxidation capability (AOC),  
131 AOC is quantified by Eq (1) (Geyer et al., 2001).

$$AOC = \sum_{i=1} k_{Y_i \rightarrow X} [Y_i] [X] \quad (1)$$

132 where  $Y_i$  are the primary pollutants (e.g., VOCs, CH<sub>4</sub>, and CO);  $X$  are atmospheric oxidants (OH, O<sub>3</sub>,  
133 NO<sub>3</sub>);  $k_{Y_i}$  are the bimolecular rate constants for the reactions of  $Y_i$  and  $X$ . A high value of AOC  
134 indicates fast scavenge of primary air pollutants. Additionally, OH reactivity ( $k_{OH}$ ), defined as the  
135 reaction rate coefficients multiplied by the concentrations of the reactants with OH, is also widely  
136 used as an indicator of AOC. The value of  $k_{OH}$  depends on both the abundances and compositions of  
137 primary pollutants and can be calculated by Eq (2).

$$k_{OH} = \sum_i k_{OH+X_i} \times [X_i] \quad (2)$$

138 where  $k_{OH+X_i}$  are the reaction rate coefficients of reaction OH+ $X_i$ ;  $X_i$  are the concentrations of  
139 pollutants (VOC, NO<sub>2</sub>, CO, OVOC etc.) (Zhu et al., 2020).

### 140 **2.3 Trend Analysis**

141 Mann-Kendall (MK) trend test is a widely used non-parametric test method (Pathakoti et al.,  
142 2021; Zhang et al., 2013). It is applicable to all distributions (that is, the data does not need to meet the  
143 assumption of normal distribution), but the data should have no serial correlation. If the data has serial  
144 correlation, it will have an impact on the significance level (p value). In this study, the MK trend  
145 analysis was performed for individual VOC concentrations during Pre-lockdown and Full-lockdown  
146 period. By using the “feast” R package, no obvious serial correlation of individual VOC is found.  
147 Therefore, the observed VOC data is suitable for MK test. Detailed description and the calculation  
148 formula of MK trend test could be found in the study of Pathakoti et al. (2021) and Alhathloul et al.  
149 (2021). A positive z value from the MK test indicates increasing trend of the target compound. On the  
150 contrary, a negative z value suggests the target compound was decreasing.

151 Sen’s slope, a non-parametric test proposed by Sen (1968), is used in this study to assess the rate  
152 of change in individual VOC concentrations. The Sen’s slope is selected since it is insensitive to  
153 outliers, and does not require a normal distribution of residuals. Sen’s slope (Q) is mathematically  
154 represented by the following equations.

$$Q = \text{median}(SS_{ij}) \quad (3)$$

$$SS_{ij} = \frac{x_j - x_i}{j - i}, 1 \leq i \leq j \leq n \quad (4)$$

155 where  $x_j$  and  $x_i$  are concentrations of VOC specie  $x$  at time  $j$  and  $i$  ( $1 \leq i \leq j \leq n$ ), respectively.  $SS_{ij}$  is the  
156 linear slope between time  $i$  and  $j$ , and  $Q$  is the median of  $SS_{ij}$ . Positive and negative  $Q$  values indicate  
157 increasing or decreasing trend of VOC specie  $x$ , respectively.

## 158 **2.4 Deweathered model**

159 The observed concentrations of  $O_3$  could be influenced by meteorological conditions, emissions  
160 and/or chemistry. The emissions and chemistry are being treated together and separated from  
161 meteorology by the deweathered approach based on the random forest (RF). Hourly data of Unix date  
162 (number of seconds since 1970-01-01), Julian day, weekday, hour of day, wind speed (WS), wind  
163 direction (WD), temperature (T), relative humidity (RH), and pressure (P), which are available during  
164 the whole observation, were used for the deweathered calculation of  $O_3$ . The missing data was  
165 replaced by linear interpolation. Training of the models was conducted on 80% of the input data and  
166 the other 20% was withheld from training. To avoid the disadvantage of overfitting during the training  
167 of RF, a process called bagging (or bootstrap aggregation) was adopted. Bagging results in new,  
168 sampled set called out-of-bag (OOB) data. A decision tree is then grown on the OOB data. Therefore,  
169 all the decision trees are grown on different observations and avoid the overfitting (Grange and David  
170 (2019)). To determine the value of number of trees (ntree), number of samples (nsample), and the  
171 minimal node size, a series of random forests were performed under different choices of ntree,  
172 nsample, and minimal node size. The results suggest that the highest coefficient of determination ( $R^2$ ,  
173 0.84) was obtained when ntree, nsample and minimal node size was set as 300, 300, and 5,  
174 respectively (Table S1 and S2). More details of this model could be found in the study of Grange and  
175 David (2019). The uncertainty of the deweather model is obtained by growing 50 random forest  
176 models with the hyperparameters described above, which is the same method as Grange and Carslaw  
177 (2019). The mean and standard error of the predicted  $O_3$  concentrations is shown in Figure S1, and  
178 results of the model are stable during the 50 runs. The differences in observed  $O_3$  concentrations  
179 ( $O_{3,Obs}$ ) and deweathered  $O_3$  concentrations ( $O_{3,Normal}$ ) were regarded as the concentrations contributed

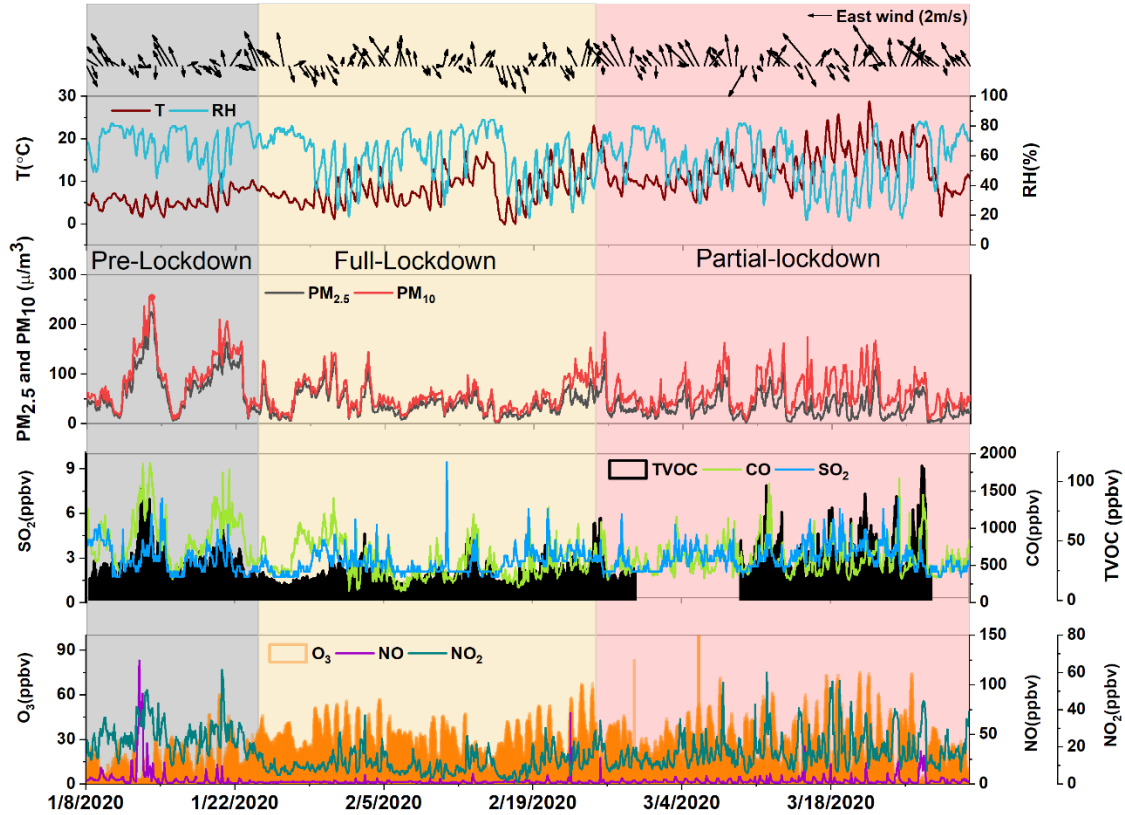


180 by meteorology ( $O_{3, \text{Met}}$ ), which is consistent with the definition in Li et al. (2021). Correspondingly,  
181 the differences in  $O_{3, \text{Normal}}$  concentrations in different periods represent the influence of emissions,  
182 since the  $O_{3, \text{Normal}}$  has already removed the influence of meteorological conditions.

### 183 **3. Results and discussion**

#### 184 **3.1 Overview of the field campaign**

185 Figure 2 shows the meteorological conditions during the observation. During the whole  
186 experiment, the prevailing WD was southeast. The average T and RH was  $9.9 \pm 5.1^\circ\text{C}$  and  $58.9 \pm$   
187  $17.1\%$ , respectively. Compared to Pre-lockdown period, the concentrations of  $\text{PM}_{2.5}$ ,  $\text{PM}_{10}$ ,  $\text{SO}_2$ ,  $\text{NO}$ ,  
188  $\text{NO}_2$ , TVOC and CO during Full-lockdown period decreased by 48%, 42%, 11%, 65%, 58%, 33% and  
189 39%, respectively. It should be noted that the decreasing ratio of  $\text{VOC}/\text{NO}_x$  is around 1.75, suggesting  
190 that the lockdown policy has stronger influence on  $\text{NO}_x$  emissions than VOC emissions. The  $\text{O}_3$   
191 concentrations during the same period in 2020 and 2019 are summarized in Table 2. Considering the  
192 influence of Chinese New Year, the corresponding period in 2019 was decided according to lunar  
193 calendar. It should be noted that, compared to Full-lockdown period in 2019, the mean  $\text{O}_3$   
194 concentration in 2020 is obviously higher (5.5 ppbv, Figure 2). Meanwhile, the average  $\text{O}_3$   
195 concentrations in Full-lockdown period in 2020 was 67% higher than that during Pre-lockdown period  
196 in 2020. To roughly analyze the cause of the obvious increase of  $\text{O}_3$  during Full-lockdown period in  
197 2020, we summarized the temperature (T) and relative humidity (RH) in Table 2. The T and RH in  
198 Full-lockdown period in 2020 was  $\sim 1.6^\circ\text{C}$  higher and 6.1% lower than that in the same period in 2019,  
199 while the P and WS were comparable during the same period in 2020 and 2019 (Table 2). The  
200 relatively higher T was in favor of  $\text{O}_3$  formation during the Full-lockdown period in 2020. As for RH,  
201 the influence on  $\text{O}_3$  is nonlinear (Zhang et al., 2020), and based on our sensitivity test, lower RH could  
202 lead to decrease or increase of  $\text{O}_3$  concentration (Figure S2). Overall, changes in  $\text{O}_3$  concentrations  
203 could be a result of the joint effect of meteorological conditions and emissions/chemistry, the  
204 following sections would discuss these influences respectively.



205

Figure 2 Time series of meteorological parameters and air pollutants during the whole observation.

206

207

Table 2 Comparison of average meteorological conditions during Pre-lockdown, Full-lockdown, and Partial-lockdown in 2020 and the same period in 2019.

208

Periods	Date	P (hPa)	RH (%)	T (°C)	Precipitation (mm)	WS (m/s)
Pre-lockdown	(2020.1.8-1.24)	1025.4	84.9	4.8	0.13	1.8
Same period in 2019	(2019.1.19-2.4)	1025.6	72.7	5.2	0.05	1.9
Full-lockdown	(2020.1.25-2.24)	1025.6	73.0	7.3	0.09	2.1
Same period in 2019	(2019.2.5-3.7)	1024.1	79.1	5.7	0.15	2.1
Partial-lockdown	(2020.2.25-3.31)	1018.9	69.5	12.1	0.11	2.4
Same period in 2019	(2019.3.8-4.12)	1017.6	64.0	13.8	0.02	2.0

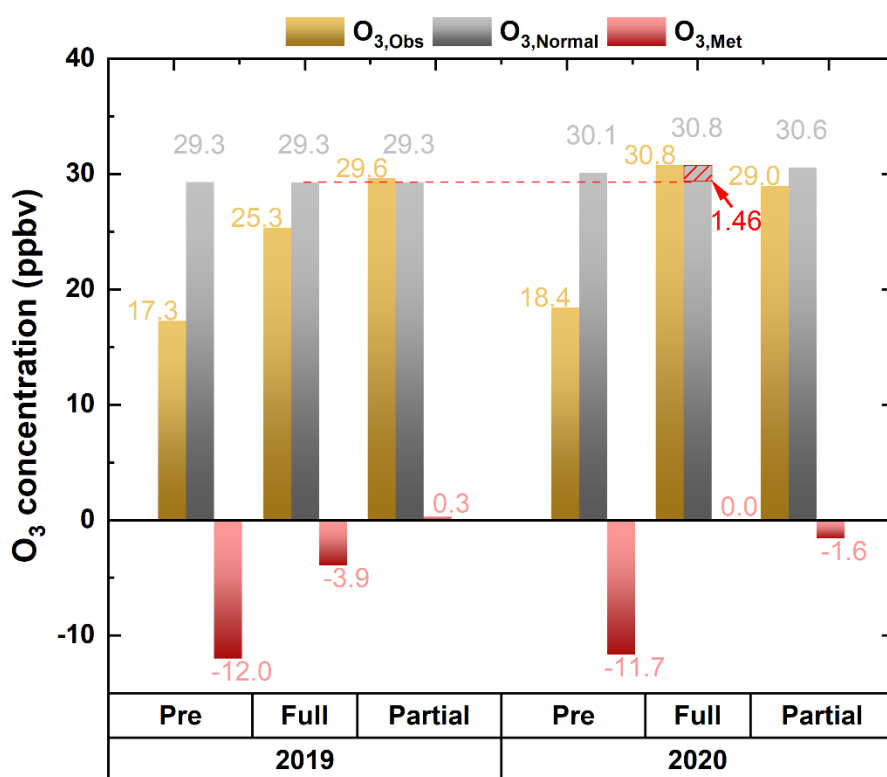
209

### 210 3.2 Mechanism affecting the obvious O<sub>3</sub> increase

#### 211 3.2.1 Meteorological perspective

212 Deweathered O<sub>3</sub> concentrations were calculated based on the model described in Section 2.4. The  
 213 difference between O<sub>3,Obs</sub> and O<sub>3,Normal</sub> can be regarded as the meteorological influence (O<sub>3,Met</sub>). In

214 addition, the difference between  $O_{3,Normal}$  concentrations in different years could be considered as the  
 215 influence of emissions ( $O_{3,Emi}$ ). Figure 3 exhibited the average  $O_{3,Obs}$ ,  $O_{3,Normal}$ ,  $O_{3,Met}$  during the same  
 216 periods in 2019 and 2020, respectively. It is obvious that the  $O_{3,Obs}$  during Pre-lockdown period is  
 217 much lower than that during Full-lockdown period in both years, which was partly attributed to  
 218 negative influence of meteorological condition during Pre-lockdown period (Figure 3). This is  
 219 consistent with the increasing temperature and solar radiation, which could significantly contribute to  
 220 the increase in ozone concentration, from Pre-lockdown to Full-lockdown period. It should be noted  
 221 that meteorology constrained  $O_3$  concentrations by 3.9 ppbv during the Full-lock down period in 2019.  
 222 Apart from the influence of meteorological condition, the  $O_{3,Normal}$  in Full-lockdown period in 2020 is  
 223 still 1.46 ppbv and 0.64 ppb higher than that during Full-lockdown period in 2019 and that during Pre-  
 224 lockdown period in 2020, indicating that improper decline of precursor emissions was possibly the  
 225 key reason for the obvious increase of  $O_3$  during Full-lockdown period in 2020.



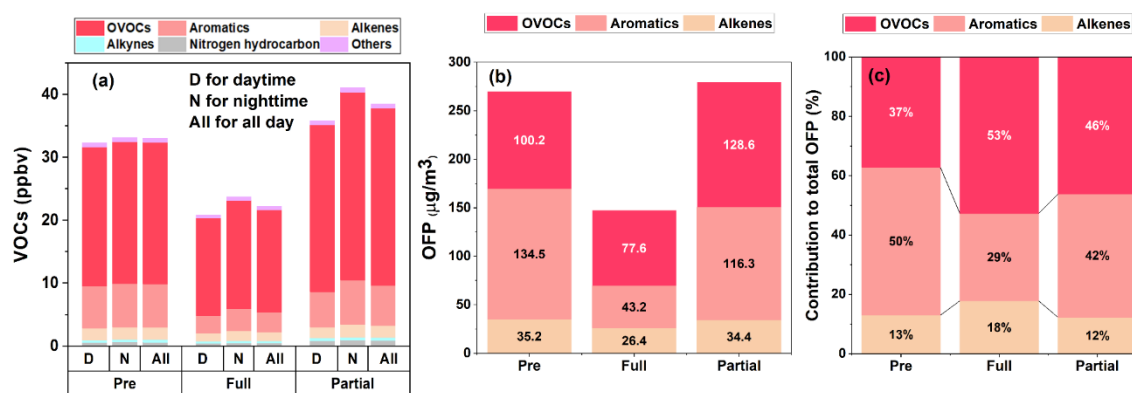
226  
227

Figure 3. Comparison of observed (Obs), weather-normalized (Normal), and meteorological-factors-infected

228

(Met) O<sub>3</sub> concentrations during the same period in 2019 and 2020.229 **3.2.2 Ambient VOCs**

230 As mentioned above, the changes in O<sub>3</sub> precursor emissions strongly affected the O<sub>3,Obs</sub>, and the  
 231 changes in VOCs and NO<sub>x</sub> emissions would eventually be reflected by the observed concentrations of  
 232 individual VOCs and NO<sub>x</sub>. Therefore, the concentrations of each VOC group in different periods were  
 233 summarized (Figure 4). OVOCs dominated the total VOCs (TVOC) concentrations during the whole  
 234 observation, with a daily average concentration of 21.44 ± 10.27 ppbv. During Full-lockdown period,  
 235 the TVOC dropped to 22.19 ± 7.9 ppbv from 32.78 ± 13.81 ppbv, which was mainly affected by the  
 236 decrease in industrial activities and traffic volume. This is proved by the trend of traffic volume,  
 237 VOCs emission and traffic/industrial-derived VOCs (Text S1 and Figure S3). In addition, Jensen et al.  
 238 (2021) found the VOC emissions from most industries in Changzhou share the same “U-shape” trend  
 239 as our study. The most obvious drop was found in aromatics (~54%), followed by OVOCs (~27%),  
 240 alkenes (~26%), nitrogen hydrocarbon (~25%), and other VOCs (~21%). Additionally, the  
 241 discrepancy of daytime and nighttime VOCs concentrations during different periods were compared  
 242 (Figure 4 (A)). The concentration of each VOCs group exhibited higher values during nighttime,  
 243 which was caused by the low atmospheric oxidation condition and the low atmospheric boundary  
 244 layer height (Maji et al., 2020; Valach et al., 2015).



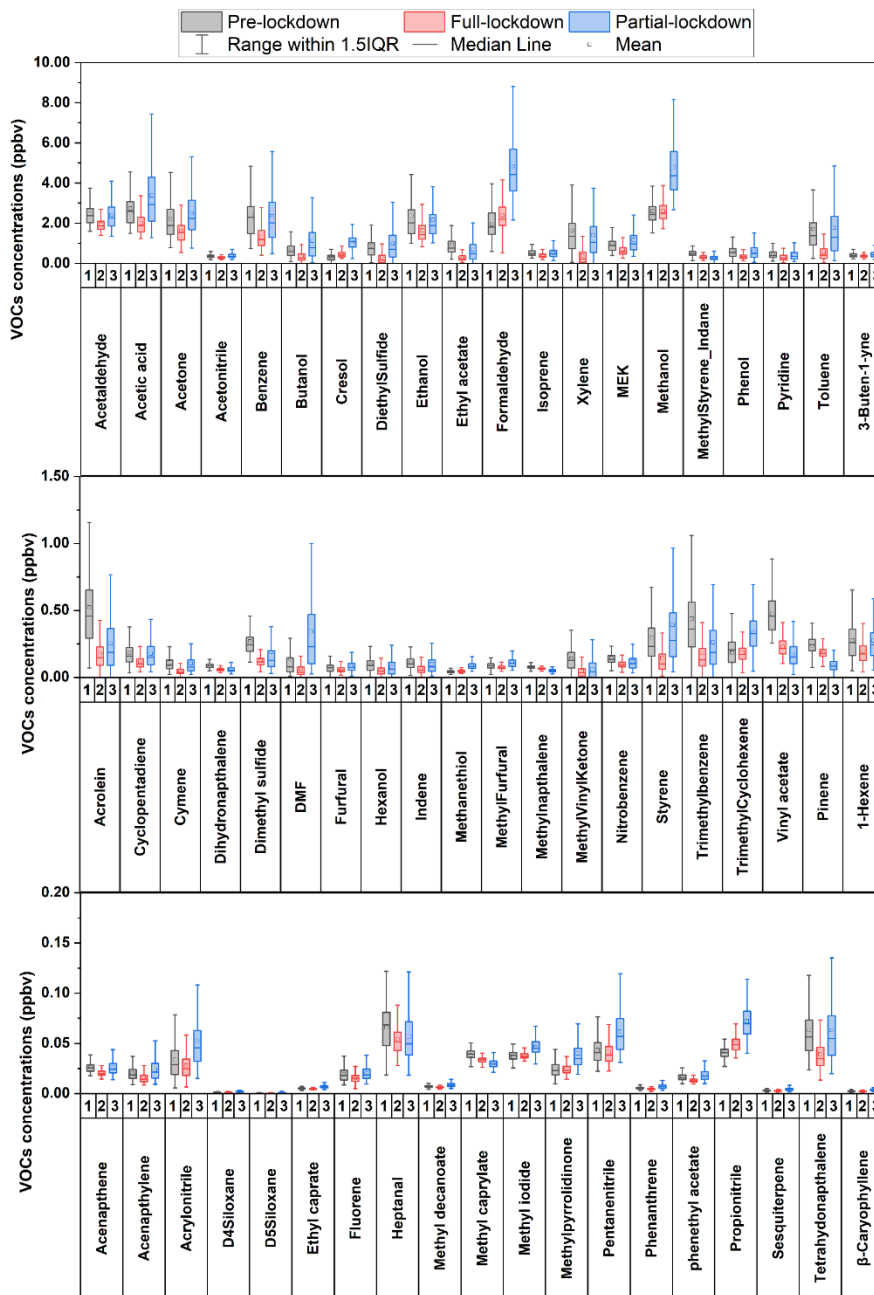
245

246 **Figure 4. Comparison of daytime and nighttime VOCs concentrations (A), average OFP (B), and contribution**  
 247 **to total OFP (C) during different periods.**

248 Furthermore, the average concentrations of individual VOCs during different periods were

249 summarized in Figure 5. Total 42 VOC species exhibited an ‘U’ shape trend during the whole  
250 observation, while formaldehyde (HCHO) and methanol showed an obvious increasing pattern. It  
251 should be noted that the measurement of HCHO could be strongly influenced by humidity. Since  
252 within the drift tube, the back reaction, which converse the protonated HCHO back into HCHO, is  
253 highly humidity dependent (Inomata et al., 2008; Warneke et al., 2011).

254 To quantitatively evaluate the changes of individual VOC concentrations from Pre-lockdown to  
255 Full-lockdown period, when the variations of each VOCs are obvious, we applied MK trend test and  
256 Sen’s slope analysis based on the hourly average VOCs concentration data (Table S3). Table 3 lists the  
257 top 10 VOCs species with decreasing pattern (with negative Q value) from Pre-lockdown to Full-  
258 lockdown period. Toluene, benzene and xylene exhibited the most significant decreasing pattern, with  
259 a slope of  $7.73 \times 10^{-4}$ ,  $7.36 \times 10^{-4}$ , and  $7.20 \times 10^{-4}$  ppbv h<sup>-1</sup>, respectively. As for NO<sub>x</sub> and TVOC, the slope  
260 was  $-1.62 \times 10^{-2}$  and  $5.48 \times 10^{-3}$  ppb h<sup>-1</sup> (Table S3). This result is consistent with the drastic drop of  
261 industrial activities and traffic volumes, which are key sources of aromatics and NO<sub>x</sub>, from Pre-  
262 lockdown to Full-lockdown period. Other VOCs, such as ethyl-acetate, acetic acid, acetaldehyde,  
263 diethyl sulfide, ethanol, butanol and acrolein are also tightly associated with industrial processes,  
264 thereby showed decreasing trend from Pre-lockdown to Full-lockdown period. Additionally, the  
265 average diurnal variations of acetonitrile, dimethyl formamide (DMF), and styrene, which are tracers  
266 of biomass burning and industrial emission, respectively, exhibited significant reduction during Full-  
267 lockdown period (Figure S4), also indicating strong decrease in these emissions. However,  
268 formaldehyde and methanol exhibited increasing trend, with a slope of  $12.78 \times 10^{-4}$  and  $6.35 \times 10^{-4}$  ppbv  
269 h<sup>-1</sup>, respectively. This could be explained by the secondary formation of HCHO and methanol, which  
270 was promoted under better oxidation condition in Full-lockdown period.



271

272

Figure 5. Concentrations of individual VOC species during different period.

273

\*MEK, DMF, are abbreviation of Methyl ethyl ketone and dimethylformamide, respectively.

274

275

276

277

278

**Table 3. Top 10 VOCs with decreasing trend from Pre-lockdown to Full-lockdown**

VOC	Z value	Q *10000 (ppbv h <sup>-1</sup> )	VOC	Z value	Q *10000 (ppbv h <sup>-1</sup> )
Toluene	-14.02	-7.73	Acetaldehyde	-10.31	-3.95
Benzene	-9.65	-7.36	Diethyl sulfide	-9.15	-3.16
xylene	-12.38	-7.20	Ethanol	-5.48	-3.09
Ethyl-acetate	-18.53	-5.20	Butanol	-10.42	-2.83
Acetic acid	-6.79	-4.12	Acrolein	-15.48	-2.76

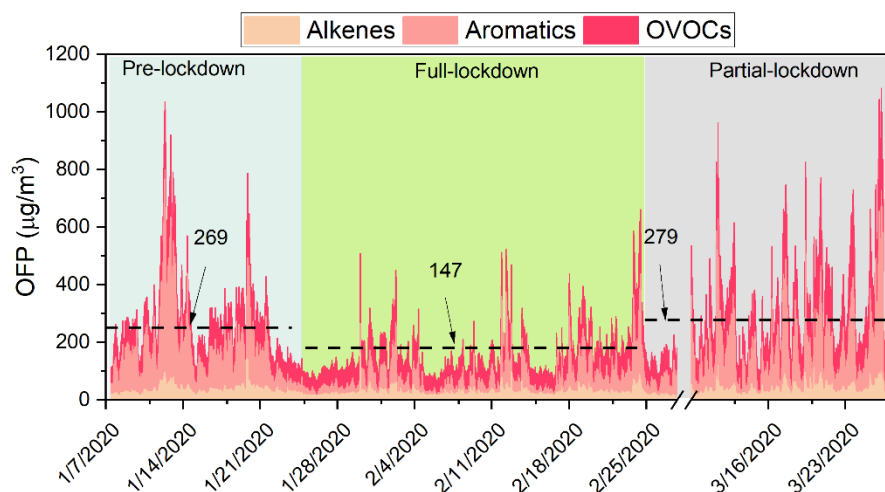
### 280 3.2.3 Chemistry perspective

281 The reactivities of different VOCs vary significantly, hence, ozone formation potential (OFP) is  
 282 used in this study to assess the potential contribution of active VOCs (including alkenes, aromatics  
 283 and OVOCs) to O<sub>3</sub> formation on the same basis, and it can be calculated by formula (5):

$$OFP_i = MIR_i \times [VOC_i] \quad (5)$$

284 where  $MIR_i$  is the ozone formation potential coefficient for a given VOC species  $i$  in the maximum  
 285 increment reaction of O<sub>3</sub>, acquired from Carter (2009);  $[VOC_i]$  is the concentration of VOC species  $i$   
 286 (in  $\mu\text{g}/\text{m}^3$ ). It should be noted that OFP does not indicate O<sub>3</sub> concentration but only serves as a  
 287 reference for the potential O<sub>3</sub> produced via the degradation of VOCs. The time series of total OFP is  
 288 shown in Figure 6. The average OFP in Pre-lockdown, Full-lockdown, and Partial-lockdown period  
 289 was  $269.4 \pm 146.0$ ,  $147.2 \pm 72.4$ ,  $279.3 \pm 168.6 \mu\text{g}/\text{m}^3$ , respectively. The trend of the total OFP  
 290 indicates the drastic decrease of VOCs reactivities from Pre-lockdown to Full-lockdown period.  
 291 During Pre-lockdown period, aromatics were the dominant OFP contributor (49%), followed by  
 292 OVOCs (38%) and alkenes (13%) (Figure 4). Among VOCs, xylene exhibited the maximum OFP  
 293 value ( $68.6 \pm 59.3 \mu\text{g}/\text{m}^3$ ), followed by acetaldehyde ( $28.8 \pm 6.4 \mu\text{g}/\text{m}^3$ ), toluene ( $25.7 \pm 20.1 \mu\text{g}/\text{m}^3$ )  
 294 trimethylbenzene ( $25.4 \pm 15.8 \mu\text{g}/\text{m}^3$ ), and formaldehyde ( $22.7 \pm 9.1 \mu\text{g}/\text{m}^3$ ) (Figure S5). Compared to  
 295 Pre-lockdown period, the OFP of aromatics decreased dramatically ( $-91.2 \mu\text{g}/\text{m}^3$ ) during Full-  
 296 lockdown period (Figure 4 (B)), which was mainly attributed to the rapid decline of human activities  
 297 (e.g., transportation and industry). However, the OFP of alkenes and OVOCs only decreased by 8.9  
 298 and  $22.5 \mu\text{g}/\text{m}^3$ , respectively. During the PTR-TOF-MS observation, the most abundant alkenes and  
 299 aromatics are 1-hexene and isoprene, with the  $k_{OH}$  of 100 and  $57 \times 10^{-12} \text{ cm}^3 \text{ molecule}^{-1} \text{ s}^{-1}$ ,

300 respectively (Atkinson and Arey, 2003). The fast degradation of these alkenes could attribute to the  
 301 relatively smaller change of OFP from alkenes. As for OVOCs, the secondary formation could  
 302 compensate the decrease in primary emissions. The OFP values of aromatics and alkenes during Pre-  
 303 lockdown and Partial-lockdown period are comparable, but OVOCs exhibited higher OFP  
 304 contribution (~46%) in Partial-lockdown period, which could be attributed to the higher AOC,  
 305 enhanced solar radiation and temperature during Partial-lockdown period. To compare the average  
 306 reactivity of VOCs during different periods, we calculated the mean MIR, derived by dividing the  
 307 total OFP by total VOC concentration, in each period. A higher MIR means stronger capability of  
 308 VOCs to produce ozone. As shown in Figure 7, the average MIR during Pre-lockdown, Full-lockdown,  
 309 and Partial-lockdown period was 3.85, 3.53 and 3.68 (g O<sub>3</sub>/g VOC), respectively. This result suggests  
 310 that VOC species composition in Full-lockdown is more conducive to ozone formation than that in  
 311 Pre-lockdown, and Partial-lockdown period. However, the formation of O<sub>3</sub> was sensitive to the ratio  
 312 of NO<sub>x</sub>/VOCs and meteorological conditions, which can be significantly different in each period. As  
 313 shown in Figure 7, the average NO<sub>x</sub>/VOCs ratio in the three periods (shown in) was 1.84, 0.79, and  
 314 0.84, respectively, suggesting more NO<sub>x</sub> was reduced than VOCs during Full-lockdown period, which  
 315 could further influence the sensitivity of O<sub>3</sub> formation.



316  
 317 **Figure 6. Time series of OFP during the whole observation period (dash lines represent the average OFP value**  
 318 **during each period)**



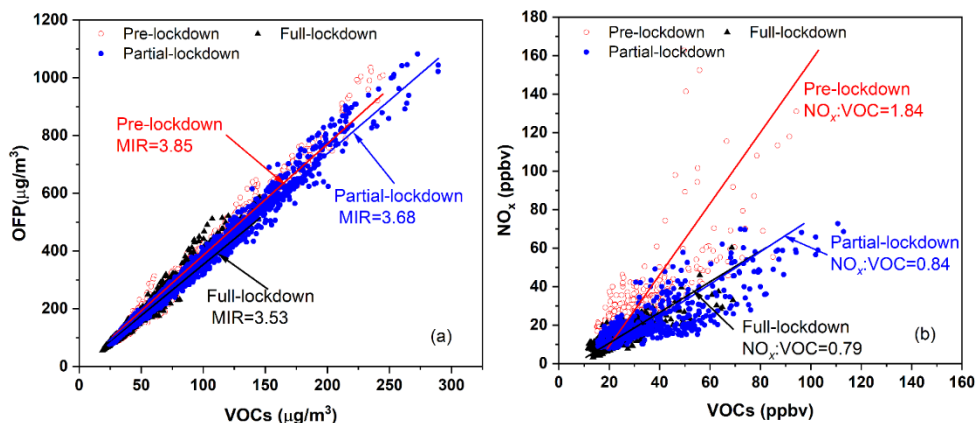
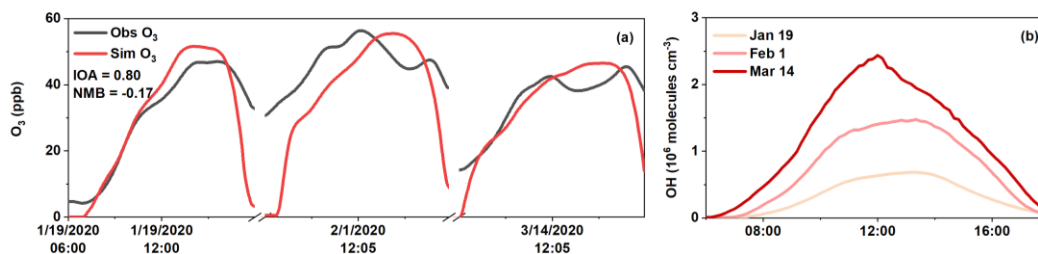


Figure 7. Plot of 1-hour averaged MIR and NO<sub>x</sub> vs VOCs during three periods.

319  
320

321 To investigate the detailed formation mechanism of O<sub>3</sub> in each period, three cases (January 19<sup>th</sup>,  
322 February 1<sup>st</sup>, March 14<sup>th</sup>) with stagnant meteorological conditions were chosen. The index of  
323 agreement (IOA) of O<sub>3</sub> is 0.80, indicating that the model can capture the daytime variation of O<sub>3</sub>. The  
324 simulated daytime OH concentrations exhibited an increasing trend from January 19<sup>th</sup> to March 14<sup>th</sup>,  
325 with an average value of  $0.36 \pm 0.27 \times 10^6$ ,  $0.75 \pm 0.54 \times 10^6$  and  $1.18 \pm 0.78 \times 10^6$  molecules cm<sup>-3</sup>,  
326 respectively. This could be attributed to the increasing solar radiation and temperature from January to  
327 March. To analyze the atmospheric oxidation, we calculated the AOC according to Eq(1). The average  
328 daytime AOC on Jan 19<sup>th</sup>, Feb 1<sup>st</sup>, and Mar 14<sup>th</sup> was  $0.26 \pm 0.35$ ,  $0.23 \pm 0.33$ , and  $0.31 \pm 0.38$   
329 molecules cm<sup>-3</sup> s<sup>-1</sup>, respectively (Figure 9). Comparatively, these values are much lower than those  
330 simulated for Shanghai and Beijing (Liu et al., 2012; Zhu et al., 2020; Zhang et al., 2021) in summer,  
331 mainly due to the meteorological conditions in winter season. It is notable that the simulated OH on  
332 Jan 19<sup>th</sup> was significantly lower than that on Feb 1<sup>st</sup>, but the AOC on Jan 19<sup>th</sup> was comparable to that  
333 on Feb 1<sup>st</sup>. This should be ascribed to the abundant primary pollutants, which efficiently react with OH,  
334 during Pre-lockdown period.

335



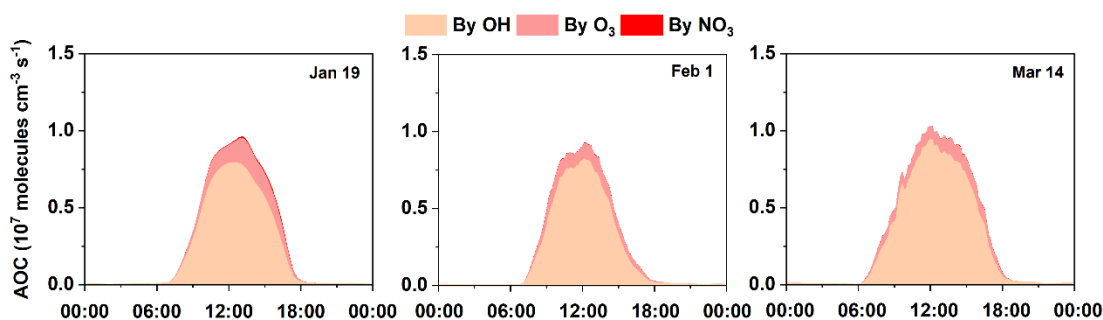
336

337

Figure 8. Comparison of simulated and observed O<sub>3</sub> (a) and simulated daytime OH concentrations (b) in three

338

cases.



339

340

Figure 9. Diurnal variation of AOC in three cases

341

The daytime variations of OH reactivity calculated by OBM model are exhibited in Figure 10,

342

including the contribution from measured pollutants (e.g., VOCs, NO<sub>x</sub>, and CO) and model-simulated

343

species (OVOCs). Generally, the  $k_{OH}$  assessed at Changzhou was in the range of 9~32 s<sup>-1</sup>, which was

344

comparable to that calculated for other cities in China (e.g., Shanghai 4.6~25 s<sup>-1</sup>, Zhu et al., 2020,

345

Chongqing 15~25 s<sup>-1</sup>, Tan et al., 2019 and Beijing 15~25 s<sup>-1</sup>, Tan et al., 2019). It is obvious that OH

346

reactivity peaked in the morning, with maximum values of 31.76, 17.98, and 17.30 s<sup>-1</sup>, respectively.

347

The OH reactivity from NO<sub>2</sub> exhibited obvious daytime variation, especially during the morning rush

348

hour, which lead to the peak  $k_{OH}$  value during morning. The OH reactivity ( $k_{OH}$ ) on Feb 1<sup>st</sup> was much

349

lower than that in the other two cases, which was mainly due to the abundance of emissions during

350

Pre-lockdown and Partial-lockdown period. Compared to Jan 19<sup>th</sup>, the  $k_{OH}$  from NO<sub>2</sub> on Feb 1<sup>st</sup> and

351

Mar 14<sup>th</sup> showed lower levels, with an average value of 2.62 and 3.35 s<sup>-1</sup>, respectively. This

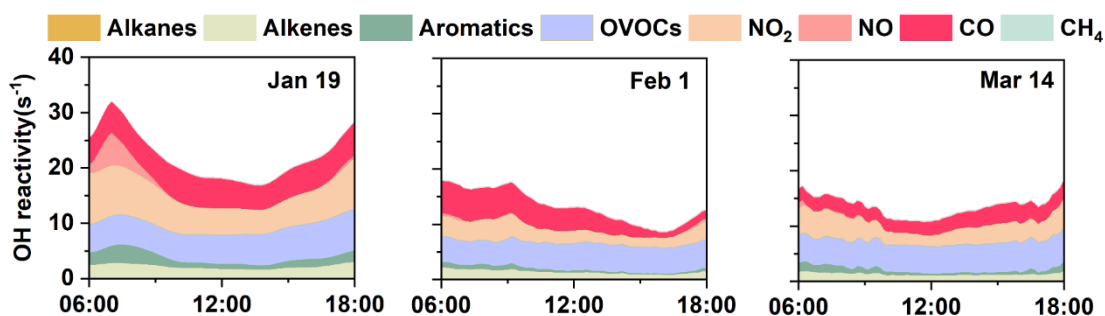
352

corresponds with the dramatic drop of traffic volume during lockdown periods. Similarly, compared to

353

Jan 19<sup>th</sup>, the  $k_{OH}$  from alkenes and aromatics were lower on Feb 1<sup>st</sup> and Mar 14<sup>th</sup>. As  $k_{OH}$  from OVOC,

354 it shared same trend as OVOC concentration, which reached the minimum value ( $5.56 \text{ s}^{-1}$ ) during the  
355 Full-lockdown period.



356

357

Figure 10. Daytime variation of OH reactivity in three cases

358

359

360

361

362

363

364

365

366

367

368

369

370

371

372

373

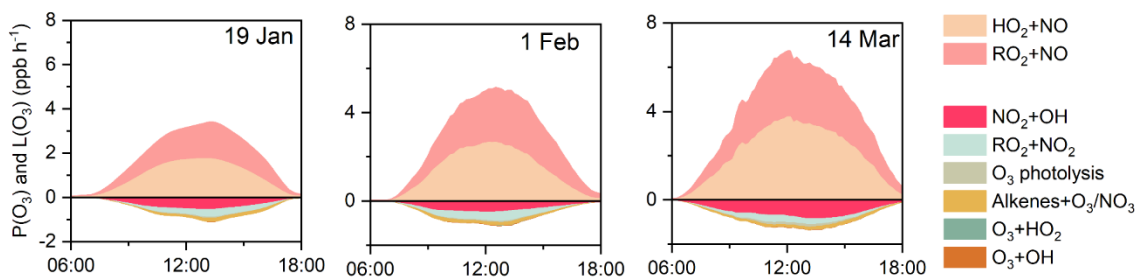
374

375

376

To investigate the variation of  $\text{O}_3$  during different periods, the formation and loss pathways of  $\text{O}_3$  were calculated (Figure 11). The formation of  $\text{O}_3$  ( $P(\text{O}_3)$ ) was dominated by  $\text{HO}_2+\text{NO}$  and  $\text{RO}_2+\text{NO}$  pathways. Although the average MIR during Full-lockdown period was the minimum among the three periods, the  $P(\text{O}_3)$  on Feb 1<sup>st</sup> was higher than that on Jan 19<sup>th</sup>. This could be attributed to the higher AOC and better photochemical conditions during Full-lockdown period. Similarly, much higher  $P(\text{O}_3)$  was found on March 14<sup>th</sup>. To avoid the influence of meteorological conditions and test the potential mean  $\text{O}_3$  (Mean $\text{O}_3$ ) concentrations under different  $\text{NO}_x/\text{VOCs}$  ratios, a series of scenario analyses were performed based on the average condition during the whole observation, and the isopleths of Mean $\text{O}_3$  concentrations are exhibited in Figure. 12. Note that the value of temperature and photolysis frequencies (J values) in the scenario analyses could be higher than the actual value during Pre-lockdown period and could further lead to overestimation of simulated Mean $\text{O}_3$  during Per-lockdown period. Additionally, the VOCs concentrations mentioned in this section only represent the VOC species in the MCM mechanism. By connecting the inflection points in each  $\text{O}_3$  isopleth, we get the ridge line, which divides the whole regime into  $\text{NO}_x$ -sensitive and VOCs-sensitive regimes (Figure. 12). During Pre-lockdown period, the  $\text{O}_3$  formation was in VOC-limited regime (triangles in Figure. 12), with an average  $\text{NO}_x/\text{VOC}$  ratio of 1.84. As for Full-lockdown period, significant decrease of  $\text{NO}_x$  and VOC emissions was observed, and the  $\text{NO}_x/\text{VOCs}$  ratio dropped to 0.79, which gradually switched the  $\text{O}_3$  formation to the junction of VOCs-limited and  $\text{NO}_x$ -limited regimes, especially on Feb 16<sup>th</sup> and Feb 17<sup>th</sup> (circles in the red rectangle in Figure. 12), when the  $\text{O}_3$  formation went into

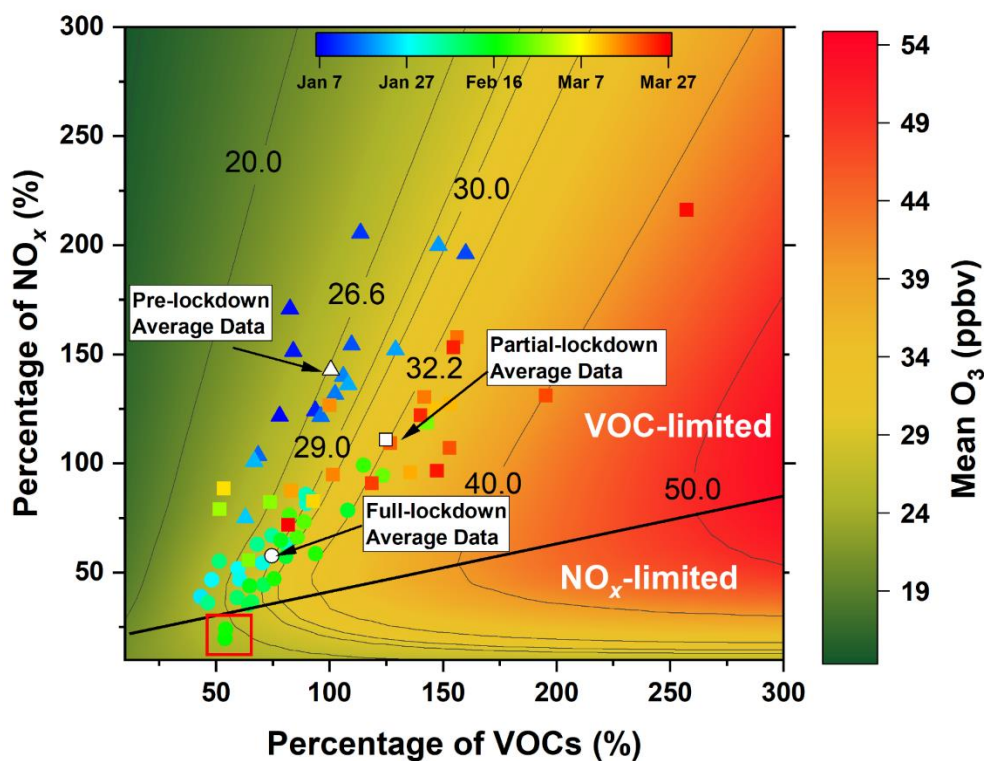
377 NO<sub>x</sub>-limited regime. During Partial-lockdown period, increasing of VOCs and NO<sub>x</sub> emission again  
 378 dragged the formation of O<sub>3</sub> back into VOCs-limited regime (triangles in Figure. 12). Interestingly,  
 379 although a great deal of NO<sub>x</sub> and VOCs emissions were diminished during Full-lockdown period, the  
 380 average MeanO<sub>3</sub> in Full-lockdown was supposed to be 2.4 ppbv higher than that in Pre-lockdown  
 381 period. This result is consistent with the trend of the observed MDA8 O<sub>3</sub> and the results of the  
 382 deweathered calculation. Therefore, expect for the influence of meteorology, the improper NO<sub>x</sub>/VOCs  
 383 reduction ratio and further influence on chemistry was the key reason for the obvious increase of O<sub>3</sub>  
 384 during Full-lockdown period in Changzhou in 2020.



385

386

Figure 11. Daytime variation of P(O<sub>3</sub>) and L(O<sub>3</sub>) in three cases



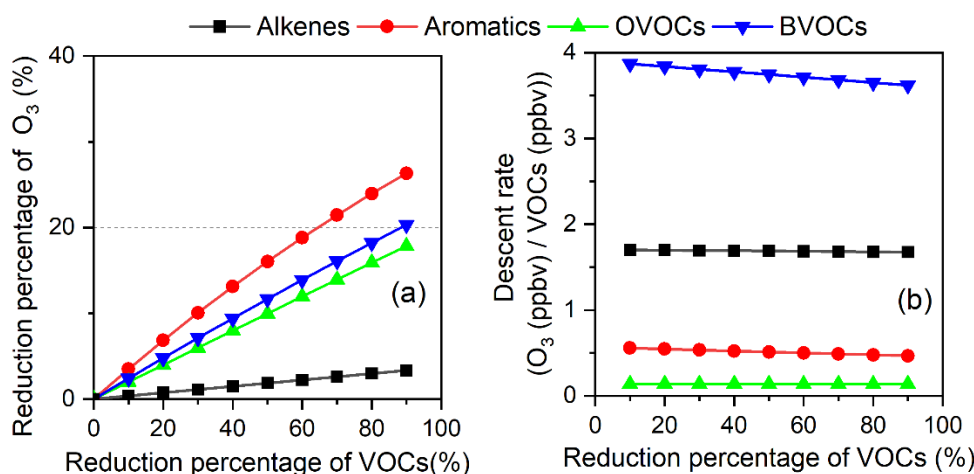
387

388 **Figure. 12 MeanO<sub>3</sub> isopleth. The colored circles, triangles, and rectangles represent the daily average**  
389 **concentrations of NO<sub>x</sub> and VOCs during Pre lockdown, Full-lockdown, and Partial-lockdown period,**  
390 **respectively. The white circle, triangle, and rectangle indicates the average NO<sub>x</sub> and VOCs concentrations**  
391 **during Pre lockdown, Full-lockdown, and Partial-lockdown period, respectively.**

392 The scenario analyses raise a question: how much O<sub>3</sub> would change as a function of reduction of  
393 NO<sub>x</sub> and VOCs? Therefore, the reduction percentage of O<sub>3</sub> ( $\Delta O_3/O_3$ ) during Pre-lockdown period as a  
394 function of reduction of VOCs and NO<sub>x</sub> were calculated, and the result could be regarded as a  
395 potential to control O<sub>3</sub> pollution. Based on the VOCs species in MCM v3.3.1, we classified the  
396 measured VOCs into four groups: alkenes (n-butene); aromatics (including benzene, toluene, phenol,  
397 xylene, styrene, cresol, and trimethylbenzene); OVOCs (including methanol, ethanol, formaldehyde,  
398 aldehyde, acrolein, methyl vinyl ketone, methyl ethyl ketone, ethyl acetate, methyl isobutyl ketone,  
399 hexanol, and heptanal); and BVOCs (isoprene, pinene, and caryophyllene). The results in Figure 13(a)  
400 indicate that more reduction potential of O<sub>3</sub> could be achieved by diminishing aromatics, followed by  
401 BVOCs, OVOCs, and alkenes. It should be noted that many light alkanes and active alkenes, such as  
402 ethene and propene, could not be measured by the PTR-TOF-MS and might further lead to the  
403 underestimation of ozone production from alkanes and alkenes. Additionally, this comparison has a  
404 drawback of being influenced by the concentrations of VOCs. To normalize the influence of  
405 concentrations of VOCs, the descent rate of O<sub>3</sub> ( $\Delta O_3$  (ppbv)/  $\Delta$ VOCs (ppbv)) as a function of  
406 reduction percentage of VOCs were calculated (Figure 13 (b)). O<sub>3</sub> exhibited the highest dependence  
407 on BVOCs, with an average descent rate of  $3.74 \pm 0.09$  ppbv/ppbv. Differing from the result in Figure  
408 13 (a), diminishing alkenes could lead to decrease of O<sub>3</sub> by an average declining rate of  $1.69 \pm 0.01$   
409 ppbv/ppbv. On the contrary, reduction of NO<sub>x</sub> would lead to increase of O<sub>3</sub>, with an average rate of  
410  $1.29 \pm 0.21$  ppbv/ppbv (Figure S6). Although the descent rate of O<sub>3</sub> turned to decrease and the  
411 sensitivity of O<sub>3</sub> formation get into NO<sub>x</sub>-limited regime when over 70% of NO<sub>x</sub> were eliminated, it  
412 still causes net increase of O<sub>3</sub>.

413 Although diminishing BVOCs seems to the most efficient way to restrain O<sub>3</sub> pollution, most of  
414 BVOCs were emitted directly from plants and could not be easily controlled. Besides, huge number of

415 OVOCs (such as formaldehyde, aldehyde, methanol, ethanol, methyl vinyl ketone, methyl ethyl  
 416 ketone, etc.) could be directly emitted from anthropogenic processes or secondary generated from the  
 417 oxidation of precursors (such as alkenes and aromatics), which complicates the control of OVOCs.  
 418 Therefore, considering the reduction potential and descent rate of O<sub>3</sub>, more efforts are needed on the  
 419 control of alkenes and aromatics.



420  
 421 **Figure 13. Reduction percentage of O<sub>3</sub> as a function of reduction percentage of VOCs (a); descent rate of O<sub>3</sub> as a**  
 422 **function of reduction percentage of VOCs (b).**

### 423 3.3 Uncertainty analysis

424 Due to limitations in the observations, several issues should be noted in the application of the  
 425 OBM model to evaluate the local chemistry in the present study. Firstly, deficiency of the observation  
 426 of C<sub>2</sub>~C<sub>5</sub> alkenes and alkanes could lead to underestimation of the simulated O<sub>3</sub>. We can only obtain  
 427 the C<sub>2</sub>~C<sub>5</sub> alkenes and alkanes concentrations from the observation during the autumn of 2018 at the  
 428 same site. To analyze the uncertainties from this disadvantage, we have done simulation by including  
 429 assumed diurnal variation of ethene, propene, butene, ethane, propane and butane which are key  
 430 C<sub>2</sub>~C<sub>5</sub> alkenes and alkanes at this site, in the model. On average, adding 0.5~2 times alkenes or  
 431 alkanes could lead to 1.65%~9.49% or 1.37~5.36% increase of simulated O<sub>3</sub>, respectively (Figure S7  
 432 and S8). In addition, the deficiency of C<sub>2</sub>~C<sub>5</sub> has potential to cause uncertainty in O<sub>3</sub> formation  
 433 potential. To quantify this impact, the EKMA analysis with the hypothetical diurnal variation of  
 434 C<sub>2</sub>~C<sub>5</sub> was also performed. Generally, adding C<sub>2</sub>~C<sub>5</sub> alkenes and alkanes in the model would lead to

435 slight increase of the simulated  $O_3$ , and could not obviously change the shape of  $O_3$  isopleth (Figure  
436 S9). Therefore, the influence of the deficiency of C2~C5 alkenes and alkanes on the  $O_3$  formation  
437 sensitivity is negligible. It should be noted that, this sensitivity analysis is based on the “hypothetical”  
438 diurnal variation of C2~C5 alkenes and alkanes, which would bring in uncertainty. We hope a wider  
439 range of VOCs would be monitored simultaneously in future field campaign and avoid this deficiency.  
440 Secondly, the photolysis frequencies (J values) were calculated as a function of solar zenith angle,  
441 altitude using lookup tables, calculated using the Tropospheric Ultraviolet and Visible (TUV) model,  
442 which could lead to uncertainty in the simulation of  $O_3$ . Hence, we analysis the influence of J values  
443 by increasing or decreasing the photolysis rates by 10% and 20%. Results showed that the simulated  
444  $O_3$  could decrease or increase by 25.14% or 21.73%, respectively, when photolysis rates were  
445 decreased or increased by 20% (Figure S10). In addition, the J values, which directly or indirectly  
446 influence the recycling of  $RO_x$ , could lead to uncertainty in the calculation of AOC and  $k_{OH}$ . Based on  
447 above sensitivity analysis, we found the relative changes in AOC and  $k_{OH}$  by 1% changes in J values  
448 was 1.07% and 0.14%, respectively. Therefore, the J values is recommended to be measured during  
449 future observations.

#### 450 **4. Conclusions**

451 After the outbreak of COVID-19, strict epidemic prevention measures have been adopted  
452 throughout China, leading to dramatic decrease in traffic volume and industrial activities. Affected by  
453 the decrease of number of vehicles on the road, non-essential industrial productivity, and associated  
454 pollutant emissions, most of the air pollutants (e.g.,  $PM_{2.5}$ ,  $PM_{10}$ , NO,  $NO_2$ ,  $SO_2$ , and VOCs) dropped  
455 to a lower level during lockdown period (especially during Full-lockdown period). However,  $O_3$   
456 increased compared to that during the same period in 2019 in many urban areas of China. To figure  
457 out the reasons for this obvious increase of  $O_3$ , the characteristics of  $O_3$  precursors ( $NO_x$ , VOCs)  
458 during Pre-lockdown, Full-lockdown, and Partial-lockdown periods in Changzhou were analyzed.  
459 Although this study was conducted in single city of China, the representativeness of Changzhou  
460 guaranteed the applicability of the results the YRD region. Results suggested that the decrease of

461 human activities during Full-lockdown period significantly suppressed the emissions of  $\text{NO}_x$  and  
462 VOCs, which further lead to dramatic drop in the concentrations of most VOCs, especially aromatics.  
463 As a result, the  $\text{NO}_x/\text{VOCs}$  ratios dropped from 1.84 at Pre-lockdown period to 0.79 during Full-  
464 lockdown period. By deweathered calculation, we found that meteorology constrained  $\text{O}_3$   
465 concentration by 3.9 ppbv during Full-lockdown period in 2019, but exhibited negligible influence on  
466 that during the same period in 2020. However, compared to Full-lockdown period in 2019, changes in  
467 precursor emissions led to 1.46 ppbv increase in  $\text{O}_3$  concentrations during the same period in 2020. To  
468 verify this result, a box model was used to simulate the formation of  $\text{O}_3$ . Results show that the AOC  
469 level during Full-lockdown was comparable to that during Pre-lockdown period, but the formation  
470 rate of  $\text{O}_3$  was much higher during Full-lockdown period. By scenario analysis, we found the decrease  
471 of  $\text{NO}_x$  and VOCs in Full-lockdown period dragged the formation of  $\text{O}_3$  from VOC-sensitive regime  
472 to the junction of VOCs- and  $\text{NO}_x$ -limited regime, and the average simulated Mean $\text{O}_3$  in Full  
473 lockdown period could be 2.4 ppbv higher than that in Pre-lockdown period. Although the  
474 deweathered model and OBM model shows differences in the emission-derived change of  $\text{O}_3$ , the  
475 results together point out that the improper reduction of  $\text{NO}_x$  and VOCs was the key reason for the  
476 obvious increase of  $\text{O}_3$  during Full-lockdown period in 2020. Overall, the outbreak of COVID-19 has  
477 caused devastation over the world. However, it provided an extreme experiment to investigate the  $\text{O}_3$   
478 formation under strict emission control policies and provided insights into the policy formulation for  
479 diminishing  $\text{O}_3$  pollution in the YRD region. The data indicate that the concentrations of VOCs and  
480  $\text{NO}_x$  have changed dramatically during the pandemic, a common situation also found in other Chinese  
481 cities, and led to the switch of  $\text{O}_3$  formation sensitivity. These results have a clear indication that, in  
482 the future, more efforts should be paid on the reduction ratio of anthropogenic VOCs and  $\text{NO}_x$ .

## 483 **Acknowledgement**

484 This study was financially sponsored by the National Natural Science Foundation of China (grant  
485 42075144, 41875161, 42005112), and the Shanghai Sail Program (no. 19YF1415600).



## 486 **References**

- 487 Alhathloul, SH., Khan, AA., Mishra, AK.. Trend analysis and change point detection of annual and  
488 seasonal horizontal visibility trends in Saudi Arabia. *Theoretical and Applied Climatology* 2021; 144:  
489 127-146.
- 490 Atkinson, R. and Arey, J.: Atmospheric Degradation of Volatile Organic Compounds, *Chemical Reviews*  
491 2003; 103, 4605–4638.
- 492 Jensen, A., Liu, ZQ., Tan, W., Dix, B., Chen, TS., Koss, A., Zhu, L., Li, Li., Gouw, J. Measurements of  
493 Volatile Organic Compounds during the COVID-19 Lockdown in Changzhou, China. *Geophysical*  
494 *Research Letters* 2021.
- 495 Carter, W. Updated maximum incremental reactivity scale and hydrocarbon bin reactivities for regulatory  
496 applications. *California Air Resources Board Contract* 2009; 339.
- 497 Cheng, Z., Zhang, J., Zhou, J., Sun, J., Zhou, W., Chen, C., Zheng, J., Wang, TJ. Air pollutant emission  
498 inventory and distribution characteristics in Changzhou (in Chinese). *The Administration and Technique*  
499 *of Environmental Monitoring* 2016; 28: 24-28.
- 500 Fan, L., Fu, S., Wang, X., Fu, Q., Jia, H., Xu, H., Cheng, J. Spatiotemporal variations of ambient air  
501 pollutants and meteorological influences over typical urban agglomerations in China during the COVID-  
502 19 lockdown. *Journal of Environmental Sciences (China)* 2021; 106: 26-38.
- 503 Fu, X., Wang, S., Zhao, B., Xing, J., Cheng, Z., Liu, H., Hao, J. Emission inventory of primary pollutants  
504 and chemical speciation in 2010 for the Yangtze River Delta region, China. *Atmospheric Environment*  
505 2013; 70: 39-50.
- 506 Gao, C., Li, S., Liu, M., Zhang, F., Achal, V., Tu, Y., Zhang, S., Cai, C. Impact of the COVID-19 pandemic  
507 on air pollution in Chinese megacities from the perspective of traffic volume and meteorological factors.  
508 *Science of The Total Environment* 2021; 773: 145545.
- 509 Geyer, A., Alicke, B., Konrad, S., Schmitz, T., Stutz, J., and Platt, U. Chemistry and oxidation capacity of  
510 the nitrate radical in the continental boundary layer near Berlin, *Journal of Geophysics Research* 2001;  
511 106, 8013–8025.
- 512 Huang, L., Liu, Z., Li, H., Wang, Y., Li, Y., Zhu, Y., Ooi, M., An, J., Shang, Y., Zhang, D., Chan., A., Li, L.  
513 The Silver Lining of COVID-19: Estimation of short-term health impacts due to lockdown in the Yangtze

514 River Delta Region, China. *GeoHealth* 2020; 4: e2020GH000272.

515 Inomata, S, Tanimoto, H, Kameyama, S., Tsunogai, U., Irie, H., Kanaya, Y., Wang, Z. J. A. C., and Physics:  
516 Determination of formaldehyde mixing ratios in air with PTR-MS: laboratory experiments and field  
517 measurements, 8, 273-284, 2008.

518 Li, L., An, J., Huang, L., Yan, R., Huang, C., and Yarwood, G. Ozone source apportionment over the  
519 Yangtze River Delta region, China: Investigation of regional transport, sectoral contributions and  
520 seasonal differences, *Atmospheric Environment* 2019; 202, 269–280.

521 Li, L., Li, Q., Huang, L., Wang, Q., Zhu, A., Xu, J., et al. Air quality changes during the COVID-19  
522 lockdown over the Yangtze River Delta Region: An insight into the impact of human activity pattern  
523 changes on air pollution variation. *Science of the Total Environment* 2020; 732:139282.

524 Li, R., Zhao, Y., Fu, H., Chen, J., Peng, M., and Wang, C.: Substantial changes in gaseous pollutants and  
525 chemical compositions in fine particles in the North China Plain during the COVID-19 lockdown period:  
526 Anthropogenic vs. meteorological influences, 21, 8677–8692, <https://doi.org/10/gkgxw6>, 2021.

527 Liu, Z., Wang, Y., Gu, D., Zhao, C., Huey, LG., Stickel, R., et al. Summertime photochemistry during  
528 CAREBeijing-2007: RO<sub>x</sub> budgets and O<sub>3</sub> formation. *Atmospheric Chemistry and Physics* 2012; 12:  
529 7737-7752.

530 Maji, S., Beig, G., Yadav, R. Winter VOCs and OVOCs measured with PTR-MS at an urban site of India:  
531 Role of emissions, meteorology and photochemical sources. *Environmental Pollution* 2020; 258: 113651.

532 Pathakoti, M., Santhoshi, T., Aarathi, M., Mahalakshmi, DV., Kanchana, AL., Srinivasulu, J., et al.  
533 Assessment of Spatio-temporal Climatological trends of ozone over the Indian region using Machine  
534 Learning. *Spatial Statistics* 2021; 43: 100513.

535 Sen, PK. Estimates of the regression coefficient based on Kendall's tau. *Journal of the American statistical*  
536 *association* 1968; 63: 1379-1389.

537 Shen, L., Zhao, T., Wang, H., Liu, J., Bai, Y., Kong, S., et al. Importance of meteorology in air pollution  
538 events during the city lockdown for COVID-19 in Hubei Province, Central China. *Science of the Total*  
539 *Environment* 2021; 754, 142227.

540 Shi, X., Ge, Y., Zheng, J., Ma, Y., Ren, X., and Zhang, Y. Budget of nitrous acid and its impacts on  
541 atmospheric oxidative capacity at an urban site in the central Yangtze River Delta region of China,

542 Atmospheric Environment 2020; 238.

543 Sun, K., Zhou, J., Ding, H., Chen, X., Liu, Z., Xue, P. Anthropogenic source VOCs emission inventory of  
544 Changzhou city (in Chinese). Environmental Monitoring and Forewarning 2019; 11: 57-62.

545 Tan, Z., Lu, K., Jiang, M., Su, R., Wang, H., Lou, SR., et al. Daytime atmospheric oxidation capacity in  
546 four Chinese megacities during the photochemically polluted season: a case study based on box model  
547 simulation. Atmospheric Chemistry and Physics 2019; 19: 3493-3513.

548 Valach, AC., Langford, B., Nemitz, E., Mackenzie, AR., Hewitt, CN. Seasonal and diurnal trends in  
549 concentrations and fluxes of volatile organic compounds in central London. Atmospheric Chemistry and  
550 Physics 2015; 15: 7777-7796.

551 Venter, ZS., Aunan, K., Chowdhury, S., Lelieveld, J. COVID-19 lockdowns cause global air pollution  
552 declines. Proceedings of the National Academy of Sciences of the United States of America 2020; 117:  
553 18984-18990.

554 Wang, W., Li, X., Shao, M., Hu, M., Tan, T. The impact of aerosols on photolysis frequencies and ozone  
555 production in Beijing during the 4-year period 2012–2015. Atmos. Chem. Phys. 19, 9413-9429 (2019).

556 Wang, W., Parrish, D., Li, X., Shao, M., Zhang, Y. Exploring the drivers of the increased ozone production  
557 in Beijing in summertime during 2005–2016. Atmos. Chem. and Phys. 20, 15617-15633 (2020).

558 Warneke, C., Veres, P., Holloway, J., Stutz, J., Tsai, C., Alvarez, S., Rappenglueck, B., Fehsenfeld, F., Graus,  
559 M., and Gilman, J. J. A. M. T.: Airborne formaldehyde measurements using PTR-MS: calibration,  
560 humidity dependence, inter-comparison and initial results, 4, 2345-2358, 2011.

561 Wolfe, GM., Marvin, MR., Roberts, SJ., Travis KR, Liao J. The Framework for 0-D Atmospheric Modeling  
562 (F0AM) v3.1. Geoscientific Model Development 2016; 9: 3309-3319.

563 Xu, L., Zhang, J., Sun, X., Xu, S., Shan, M., Yuan, Q., et al. Variation in concentration and sources of black  
564 carbon in a megacity of China during the COVID-19 pandemic. Geophysical Research Letters 2020; 47:  
565 e2020GL090444.

566 Zhang, D., Cong, Z., Ni, G. Comparison of three Mann-Kendall methods based on the China's  
567 meteorological data. Advances in Water Science 2013; 24: 490-496.

568 Zhang, K., Huang, L., Li, Q., Huo, J., Duan, Y., Wang, Y., Yaluk, E., Wang, Y., Fu, Q., and Li, L.: Explicit  
569 modeling of isoprene chemical processing in polluted air masses in suburban areas of the Yangtze River

570 Delta region: radical cycling and formation of ozone and formaldehyde, *Atmos. Chem. Phys.*, 21, 5905-  
571 5917, 10.5194/acp-21-5905-2021, 2021.

572 Zhang, K., Li, L., Huang, L., Wang, Y., Huo, J., Duan, Y., et al. The impact of volatile organic compounds  
573 on ozone formation in the suburban area of Shanghai. *Atmospheric Environment* 2020a; 232: 117511.

574 Zhang, K., Xu, J., Huang, Q., Zhou, L., Fu, Q., Duan, Y., et al. Precursors and potential sources of ground-  
575 level ozone in suburban Shanghai. *Frontiers of Environmental Science and Engineering* 2020b; 14: 1-12.

576 Zhang, P., Chen, T., Liu, J., Chu, B., Ma, Q., Ma, J., and He, H.: Impacts of Mixed Gaseous and Particulate  
577 Pollutants on Secondary Particle Formation during Ozonolysis of Butyl Vinyl Ether, 54, 3909–3919,  
578 <https://doi.org/10/gpd9p2>, 2020.

579 Zheng, H., Kong, S., Chen, N., Yan, Y., Liu, D., Zhu, B., et al. Significant changes in the chemical  
580 compositions and sources of PM<sub>2.5</sub> Wuhan since the city lockdown as COVID-19. *Science of the Total*  
581 *Environment* 2020; 739: 140000.

582 Zhu, J., Wang, S., Wang, H., Jing, S., Lou, S., Saiz-Lopez, A., et al. Observationally constrained modeling  
583 of atmospheric oxidation capacity and photochemical reactivity in Shanghai, China. *Atmospheric*  
584 *Chemistry and Physics* 2020; 20: 1217-1232.

585